IEEE Journal of Microwaves

Received 3 December 2022; revised 10 January 2023; accepted 11 January 2023. Date of publication 17 February 2023; date of current version 7 April 2023.

Digital Object Identifier 10.1109/JMW.2023.3237693

A Multioctave 8 GHz–40 GHz Receiver for Radio Astronomy

JACOB W. KOOI [1] (Senior Member, IEEE), MELISSA SORIANO[1], JAMES BOWEN[1] (Member, IEEE), ZUBAIR ABDULLA[1], LORENE SAMOSKA[1] (Senior Member, IEEE), ANDY K. FUNG [1] (Member, IEEE), RAJU MANTHENA[1], DANIEL HOPPE[1] (Senior Member, IEEE), HAMID JAVADI[1], TIMOTHY CRAWFORD [1], DARREN J. HAYTON[2], INMACULADA MALO-GÓMEZ [3], JUAN DANIEL GALLEGO-PUYOL [3] (Member, IEEE), AHMED AKGIRAY [4] (Senior Member, IEEE), BEKARI GABRITCHIDZE [5], KIERAN A. CLEARY[5], CHRISTOPHER JACOBS[1], AND JOSEPH LAZIO[1]

(Regular Paper)

[1]Jet Propulsion Laboratory, California Institute of Technology, Pasadena, CA 91106 USA
[2]Oxford Quantum Circuits, Oxford OX1 1JD, U.K.
[3]Yebes Observatory, 19141 Yebes, Guadalajara, Spain
[4]Ozyegin University, 34794 Istanbul, Turkey
[5]California Institute of Technology, Pasadena, CA 91125 USA

CORRESPONDING AUTHOR: Jacob W. Kooi (e-mail: Jacob.W.Kooi@jpl.nasa.gov).

This work was supported by the Jet Propulsion Laboratory, California Institute of Technology, through contract with the National Aeronautics and Space Administration.

ABSTRACT Accurate measurement of angular positions on the sky requires a well-defined system of reference, something that in practice is realized by the International Celestial Reference Frame (ICRF) with observations of distant (typical redshift ∼1) Active Galactic Nuclei (AGN). At such great distances a subset of these objects exhibit as little as 10−50 μas/year observed parallax or proper motion, thus giving the frame excellent spatial and temporal stability. Until fairly recently the majority of AGN centered imaging was accomplished in the S (2.3 GHz) and X (8.4 GHz) radio frequency bands, however S-band observations for reasons such as sensitivity "plateauing", increased source structure (jets), and radio frequency interference (RFI) have become less productive. Following spacecraft telemetry moves to higher frequencies and a desire to strengthen JPL's leadership in defining the next-generation of celestial reference frames has motivated the development of a "Quad-band" prototype receiver that operates in X, Ku, K, and Ka band in both right hand (RCP) and left hand (LCP) circular polarization. The goal of this receiver is to achieve less than a 20 % increase in noise over the Jansky Very Large Array (JVLA, NRAO) performance specification, which in such a wide bandwidth represents a revolutionary capability. To evaluate the various technical developments of the 8 GHz−40 GHz receiver the feedhorn optical beam was designed to interface to the US based Very Long Baseline Array (VLBA). The receiver's intermediate frequency (IF) spans 4 GHz−8 GHz, giving rise to up to eight 4 GHz IF channels for a fully populated instrument. This paper outlines the technical development of a $2^1/_2$ octave wide (8 GHz−40 GHz) X-Ka band prototype receiver, fulfilling a need for super broadband technology within the VLBI network. An important additional benefit of the wideband receiver approach is its simplicity and low cost of operation.

INDEX TERMS Astrometry, celestial reference frames, dual polarization, equalizer, HEMT, intermediate frequency (IF), IF processor, K-band, Ka-band, low noise amplifier, MMIC, quad-ridge FeedHorn, quadrature hybrid, broadband receiver, VLBI, X-band.

This work is licensed under a Creative Commons Attribution 4.0 License. For more information, see https://creativecommons.org/licenses/by/4.0/

FIGURE 1. Present global X/Ka VLBI network. JAXA's Misasa, Japan 54-meter, and ESA's Malargüe, Argentina 34-meter station are recent additions to the X/Ka network adding valuable new baselines with added sensitivity.

I. INTRODUCTION

For millennia travelers both on land and especially at sea used the stars to navigate by. We have now extended this idea to enable 'sailing' the solar system for exploring the planets. Related to that work, we use radio sources to track the motion of the planets and thus improve our knowledge of the planetary ephemeris [1], [2]. Even farther from home, the Celestial Reference Frame (CRF) [3] enables differential astrometry of the position, parallax, and proper motions of objects in our galaxy such as water masers which trace out the spiral arms of our galaxy [4]. Calibrators from the CRF are also used to phase calibrate images of other extragalactic radio sources [5]. By observing changes in the apparent positions of extragalactic sources, theories of special relativity (aberration) and general relativity via gravitational delay/'bending' [6] may also be tested.

Returning nearer to Earth, Very Long Baseline Interferometry (VLBI) signals contribute to atmospheric studies by measuring the ionosphere and troposphere. And of course, the CRF is essential to geodesy which measures both motions of the stations (tidal motions, plate tectonics) [7], and for instance astrogeodesy (the "irregular" orientation of the Earth in space) [8], [9]. Since VLBI observed Active Galactic Nuclei (AGN) are at great distances (typical redshift ∼1) the objects are stable to better than a part per billion over time scales of decades using only two parameters to describe their position. This extreme stability of the CRF objects gives a corresponding stability to the many applications of VLBI, thus providing near-absolute fiducial points on the sky for measuring angles. We note here that despite the objects extragalactic distances for many there is some detectable apparent proper motion related to, e.g., the changes in their intrinsic (jet) structure [10], or the so-called secular aberration drift caused by the rotation of the Solar System around the Galactic center [11].

In addition to CRFs, the frequency range from approximately 8 GHz to 40 GHz (also known as X band to Ka band) is of broad interest to a set of related scientific communities. A number of molecular compounds with broad astrophysical relevance have transitions within this frequency range, including methanol (CH_3OH, 12.18 GHz), water (H_2O, 22.25 GHz),

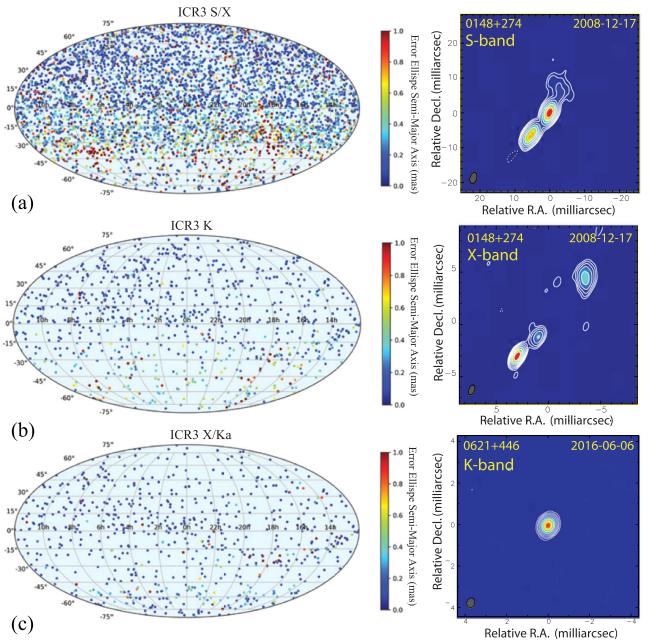

FIGURE 2. (a) Distribution of the 4536 sources included in the ICRF3 S/X band frame on a Mollweide projection of the celestial sphere. Each source is plotted as a dot, color-coded according to its position uncertainty. (b) Distribution of the 824 sources included in the ICRF3 K band frame. The data in K-band were made of 40 VLBA sessions that observed the northern sky (down to mid-southern declinations), supplemented with 16 single-baseline sessions between telescopes in Hartebeesthoek (South Africa) and Hobart (Australia) which observed sources below −15° declination. (c) Distribution of the 678 sources included in the ICRF3 X/Ka band frame. Observations were initiated in 2005 with the primary goal of building a reference frame for spacecraft navigation, now conducted on the DSN using the Ka frequency band. The data set includes a total of 168 single-baseline sessions that involved seven telescopes at the three DSN sites in Goldstone (California), Robledo (Spain), and Tidbinbilla (Australia) [14]. Right) Progressively reduced S-, X- and K-band images source structure with frequency. For K-band we use a different object as the 0148+274 source image is not available [1], noting that the general principal of reduced source structure with frequency applies.

and ammonia (NH_3, multiple lines). Deep space telecommunications, including telecommunications for lunar missions and missions near the Earth-Sun Lagrange 1 and 2 points, make use of spectral allocations near 8.4 GHz, 24 GHz, and 32 GHz. Finally, planetary radar observations conducted by the Goldstone Solar System Radar occur at frequencies close to 8.56 GHz, and there is some interest in similar observations at frequencies near ∼36 GHz.

The value of operating in K-, Ka-band [12] is such that these frequencies minimize encroaching radio frequency interference (RFI) (as opposed to 2.4 GHz C-band observations), thereby surpassing current S/X systems. In addition they have greatly reduced AGN source structure (jets), facilitate higher telemetry bandwidths, and allow tracking much closer to the sun than either S/X or optical. Missions such as Parker Solar Probe, Bepi-Columbo, and Hayabusa-2 are beginning to use Ka-band. Future missions such as Europa Clipper will rely on Ka-band for the return of science data.

In Fig. 1 we show the present X/Ka global VLBI network used by the International Celestial Reference Frame (ICRF) community. It has the highest resolution of any current

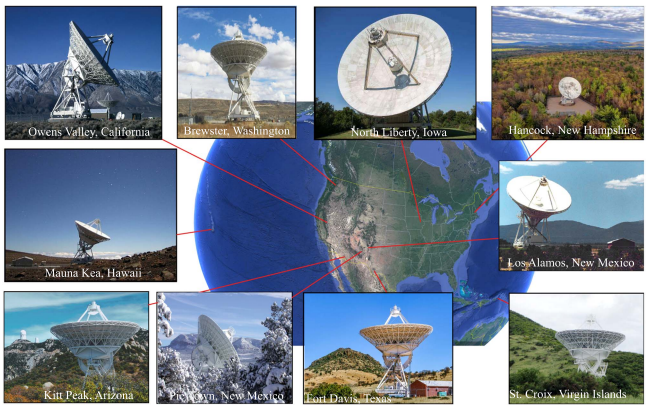

FIGURE 3. Very long baseline array (VLBA) network. The 8 GHz−40 GHz radio astronomy prototype receiver under discussion has been installed at the Owens Valley VLBA antenna (top left) given the close physical proximity to JPL, California.

astrometric technique for reference frames. The present 3rd generation International Celestial Reference Frame (ICRF3) standard [13], [14], [15] is the first frame to be realized at multiple wavelengths (S/X, K, X/Ka-bands) and in principle can tremendously benefit from the simultaneous X−Ka band dual polarization receiver discussed in this paper. The VLBI data used to build ICRF3 was acquired by arrays of 2−20 radio telescopes organized in the vast majority under the umbrella of the International VLBI Service for Geodesy and Astrometry (IVS), the very long baseline array (VLBA), and NASA's deep space network (DSN). In all, ICRF3 includes a total 4588 celestial sources, all of which are part of the S/X band catalog, 678 sources belong to the ICRF3-K and 824 sources to the ICRF3-X/Ka celestial reference frame. Fig. 2 depicts the three ICRF3 S/X, K, X/Ka reference frames (data up to spring 2018) [14]. As is evident from the example quasar outflows depicted on the right side of Fig. 2, the source structure is much reduced with increasing frequency thereby favoring (in addition to RFI mitigation) multi-frequency dual polarization X/K and X/Ka reference frame observations.

In Fig. 2, the drop in precision below $\delta = -20^{\circ}$ is due to the lack of VLBI telescopes (baselines) in the Southern Hemisphere. The median coordinate uncertainties in the S/X band catalog are 127 μas for right ascension [8] and 218 μas for declination. Compared to the S/X band catalog, the median uncertainties for the K band and X/Ka band catalogs appear to be smaller by a factor 1.5−2.

Since 2014 the U.S. Naval Observatory (USNO) has increased its support for the VLBA (Fig. 3), to the point that it now supports 50 % of the VLBA observing time, primarily for the purpose of Earth orientation and reference frame observations for terrestrial and near-Earth navigation. This has resulted in a dramatic improvement in median uncertainties in the ICRF3 catalog over the ICRF2 catalog and has motivated the development of the 8 GHz−40 GHz wideband receiver outlined in this paper.

The specifications for the multioctave "Radio Astronomy" receiver are to cover at least the frequency range 8 GHz to 36 GHz while simultaneously being within 20% of the performance of individual Jansky Very Large Array (JVLA) receivers using cryogenic low noise amplifiers (LNAs). For X-band on the VLA, this requirement corresponds to a maximum T_{rec} of 24 K, while for Ka band a $T_{rec} < 48$ K is required for an LNA-based receiver system to be attractive as a simultaneous wideband X-Ka–system for VLBI applications.

We note that the International Astronomical Union, motivated in part by the Gaia optical catalog release, is likely to adopt a new International Celestial Reference Frame (ICRF-4). This drives the need to demonstrate a $2^1/_2$ octave wideband 8 GHz−40 GHz cryogenic receiver on the VLBA network. It is noted that measurements of X and Ka band simultaneously allows for calibrations of both the Earth's ionosphere and solar plasma at the exact time and direction of the observations [16], [17]. The acquisition of data in the 8 GHz−40 GHz range consolidates X, Ku, K, and Ka band into one receiver package, saving space, power, bias complexity, and minimizes maintenance cost. By combining four receivers in one package, it also facilitates additional receivers in the various VLBI systems. Scientifically obtaining four simultaneous images would render the VLBA 4X more efficient over single band observation and enables direct comparisons of source morphology, polarization, and magnetic fields at multiple wavelengths. These performance requirements exceed anything within JPL or outside of JPL.

This paper is organized as follows: Section II introduces the X-Ka band (8 GHz−40 GHz) receiver layout. Section III describes a quad-ridged feedhorn covering $2^1/_2$ octave of bandwidth and is designed to optimally illuminate the VLBA antenna secondary mirror. Section IV details the JPL Microwave Monolithic Integrated Circuit (MMIC) effort including a custom built equalizer to allow gain shaping of the ultra wideband instrument RF bandwidth prior to being down converted to a common 4 GHz−8 GHz intermediate frequency. Section V discusses the RF front-end in more detail including a multi-octave Yebes Observatory [18] quadrature hybrid that allows translation from the feedhorn linear polarization to right and left hand circular polarization (RCP, LCP), and provides $\gtrsim$15 dB isolation between the cascaded amplifier stages. Section VI describes the backend analog IF processor which by design has a X, K (or Ka) output in two polarization's providing in principle full Stokes images of intensity & polarization for (at least) 2 bands simultaneously. Section VII details the receiver system performance as measured in the laboratory in both X and K band. And finally Section VIII gives an overview of the X-Ka band 'prototype' receiver installation at the Owens Valley VLBA antenna.

II. X-KA BAND RECEIVER LAYOUT

In this section we describe the general approach. As outlined in Section I, the receiver front-end encompasses a 5:1 frequency ratio ($2^1/_2$ octave) quad-ridge feedhorn (QRFH) [19] designed to match the optical requirement of the VLBA antenna. The output of the QRFH connects via phase matched coax lines to a 8 GHz−40 GHz custom build 90° hybrid (H1), converting the QRFH linear polarized waves to right

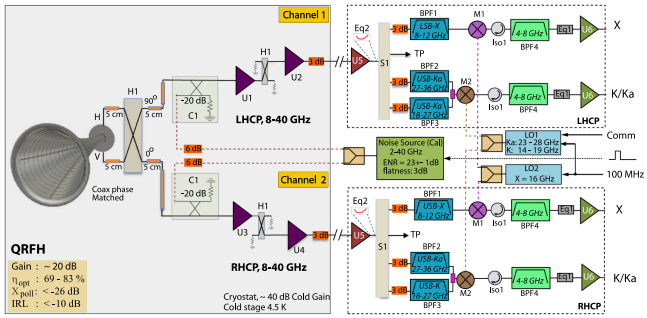

FIGURE 4. 8 GHz−40 GHz receiver layout. The 8 GHz−40 GHz front-end (*left*) constitutes a quad-ridged feedhorn, quadrature hybrid (H1) and two sets of cryogenic LNA's (U1-U4). All of these components have been custom designed for this task. The intermediate (IF) processor/down-conversion (*right*) constitutes commercial components with the exception of a 8 GHz−36 GHz custom shaped equalizer (Eq2). See text and remaining sections for detail.

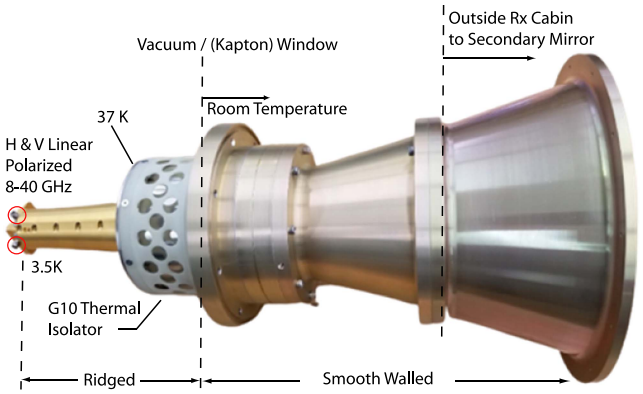

FIGURE 5. Quad-Ridge Feedhorn designed to match the VLBA 25 m antenna. The feed overall length is 495 mm, with 268 mm at atmospheric pressure. The vacuum break consists of 50 μm Kapton, which has a measured net loss of 1.25% at X-band and 2.5% at K-band. G-10, a high-pressure fiberglass laminate, is used as a cold break between room temperature and the cryostat 37 K first stage [25]. 2.92 mm K-connectors bring out the two linear polarized (red circles) orthogonal RF signals.

and left hand circular polarization (RCP, LCP). This makes the receiver compatible with the VLBA native optical design. The zero and ninety degree outputs of the quadrature hybrid route to two sets of low noise amplifiers (U1-U4). For each channel the two cascaded LNA's are "isolated" from each other by means of additional quadrature hybrids. This is important as it minimizes intermodule standing waves, and has the additional benefit of enhancing system stability. The net cryogenic gain of the cascaded amplifiers is ∼40 dB by design.

External to the cryostat there is additional 25 dB room temperature amplification (U5) prior to the signal being split four ways. Depending on the RF passband profile a gain shaping equalizer may be inserted here (Section IV-F). At the output of the 4-way power splitter custom [21] X-, K-, and Ka band bandpass filters are used to define the RF passband(s). This leaves one of the four way coupler output ports as a convenient test port, though in principle a Ku band filter may be inserted here. The bandpass filtered RF signal is down-converted (lower sideband (LSB) or upper sideband (USB)) to a common 4 GHz−8 GHz intermediate frequency (IF). Isolators and a commercial equalizers are used to band shape with final amplification via a high $P_{1\,dB}$ post IF amplifier (U6).

The local oscillator frequency needed for the down-conversion process into the 4 GHz−8 GHz IF band is 16 GHz for X-band (LSB-IF), 14−19 GHz for K-band (USB-IF), and 23−28 GHz for Ka-band (LSB-IF). In the case of the Owens Valley VLBA installation we interface to a common 15.8000 GHz tone from one of the observatory's synthesizers.

III. QUAD-RIDGE FEEDHORN

In this section we describe the quad-ridge feedhorn design and measured results. An annotated photo of the feed is shown in Fig. 5. The feed is very similar to those described in [19], [20]. The major design requirements for the feed are specified in Table 1 with the frequency of operation chosen to cover the required 8 GHz−40 GHz science as described earlier. While the feed is natively linear polarized, a single broadband 90° hybrid translates this to two orthogonal circular components over the entire 5:1 frequency band. The return loss

TABLE 1. Key Feed Requirements

Frequency	8 GHz−40 GHz
Polarization	Dual Linear
Return Loss	$>$ 10 dB
Beam Width	Secondary subtends half angle of 13.3°
f/D	2.11

requirement for a broadband feed of this type is commensurate to that of the broadband LNA input return loss performance. The feed beam width is dictated by the target antenna, in this case the VLBA dual-shaped 25 m Cassegrain antenna, [22]. Analysis of the feed was carried out in the time domain mode, using the commercial tool CST [23]. And as described later, the feed profile and aperture size have been tuned to provide maximum efficiency for a simplified, symmetric version of the VLBA shaped antenna using GRASP [24] computed feed beam patterns.

Fig. 6 shows the mechanical construction of the feed. The feed is a quad-ridged feedhorn is similar to [19] in order to provide high bandwidth. Introduction of the quad-ridge section allows the feed to cover the 5:1 bandwidth, whereas a standard circular waveguide horn is limited to approximately a 2:1 bandwidth ratio. The quad-ridges allow higher order modes thereby increasing the effective bandwidth. The horn is constructed in several sections with the quad-ridged portion fabricated in quadrants. The quad-ridged fins are smoothly terminated prior to the thermal break allowing for a simple vacuum window implementation. Truncation of the quad-ridged section in this manner was found to have minimal effect the simulated radiation patterns. A thin 50 μm Kapton window is installed just above the thermal break to separate the vacuum portion of the horn from the larger smooth-walled portion. An additional large diameter Kapton 50 μm window has been placed over the horn aperture at the VLBA Antenna to weatherproof the feed.

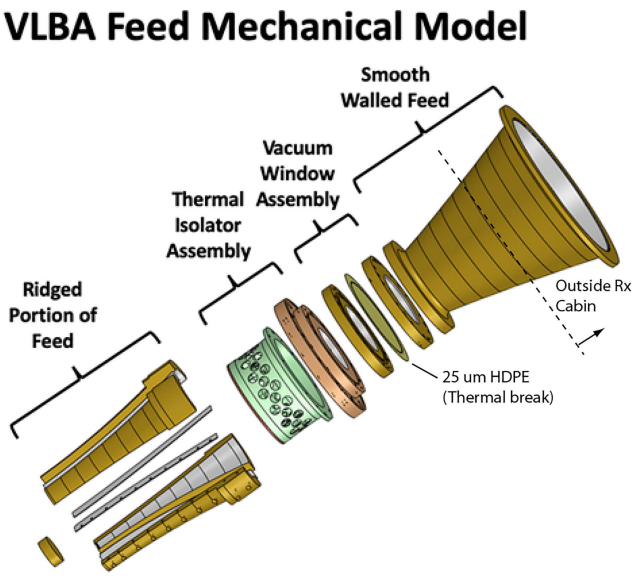

FIGURE 6. VLBA quad-ridged feed, exploded view showing the various sections.

The second major requirement on the feed performance is the radiation pattern quality. Besides beam width requirement shown in Table 1 phase center stability over the large frequency band is also a concern. For this type of feed design at lower frequencies the phase center tends to move further away from the base of the feed. In this case, the phase center at 8 GHz is ∼263 mm away from the base whereas the phase center at (for example) 36 GHz is at 119 mm from the base. For maximum efficiency the feed antenna focus has to be lined up with the focal point of the secondary mirror of the VLBA. Simulations show that aligning the feed antenna at the VLBA secondary focus corresponding to the 32 GHz phase center gives maximum overall efficiency. Example measured and computed radiation patterns for the feed at the band edges, 8 and 36 GHz, are shown in Fig. 7. In both cases good agreement between the measured and computed patterns is seen. Similar agreement was found for selected frequencies across the operational band.

A GRASP 25 m VLBA antenna model, including the antenna's secondary mirror, was created with the computed quad-ridge feed patterns as computed by CST used in this model. Fig. 8(a) shows the computed aperture efficiency (black curve) over the operational frequency band. Greater than 70% efficiency is achieved secondary focus fixed at the 32 GHz horn phase center position) except at the very lowest edge of the band. 75% is achieved over most of the band. Also plotted are the maximum efficiency achievable with the feed ignoring inefficiency due to phase errors and mismatched beam shape relative to the ideal pattern for which the antenna was shaped (red), spillover efficiency (brown), and inefficiency due to loss of power in higher order azimuthal modes (blue). At low frequencies the efficiency is driven by spillover and phase error. At high frequency efficiency is limited by beam shape and to some extent phase error. To circumvent the phase error, for single RF band (non

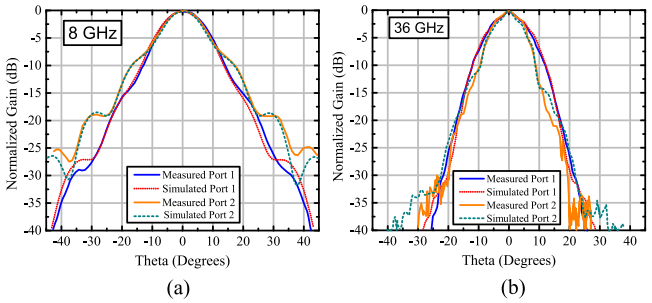

FIGURE 7. QRFH simulated (dotted) and measured (solid) feed patterns. (a) 8 GHz, (b) 36 GHz.

simultaneous) observations the feedhorn aperture efficiency can be peaked up by a slight motion of the antenna secondary mirror (z-direction).

Fig. 8(b) shows the measured return loss for the feed from 8 GHz–40 GHz in each of the two linearly polarized ports. The requirement of −10 dB is met across the required bandwidth with the return loss rapidly rising for frequencies below 8 GHz as the dominant TE_{11} mode approaches cutoff.

As was discussed above, while the feed is linearly polarized there is a strong desire to create circularly polarized outputs from the receiver. The conversion is accomplished by combining the X/Y linear polarization in a broad band quadrature hybrid prior to the first LNA. The performance of the hybrid is discussed in detail in a later section of the paper. Both the relative phase and amplitude of the X and Y paths contribute to the circular cross polarization. Phase errors in the path are caused by the fact that the X and Y probes in the throat of the feed are physically located in different planes. In addition, the rearmost probe's field must traverse the first probe causing a perturbation in its phase. Finally, path length errors in the hybrid mean that perfect quadrature cannot be maintained across this wide band. Fig. 8(c) shows a calculation of the net phase and amplitude error between the X and Y channels considering these effects. In this case cable length adjustment was used to compensate for any linear component of phase error present across the band. The residual phase errors are limited to $\lesssim$ +/- 3.0 degrees around a nominal value of −93.5 degrees, while the amplitude errors are between +0.6 and −0.6 dB from 8 GHz–40 GHz. The feed and hybrid contribute roughly the same amount of amplitude error. Fig. 8(d) shows the net cross polarization (CP) resulting from the above linear channel errors. The mean computed QRFH cross polarization level is level of approximately −28 dB, the worst case level being approximately -24 dB, both of which are satisfactory for the discussed celestial reference frame application.

IV. ULTRA-WIDEBAND MMIC DESIGN

We have developed multi-octave bandwidth cryogenic low noise amplifier modules, spanning X through Ka band. Of interest are radio astronomy applications such as the Next Generation Very Large Array [26], and future instruments with multi-octave bandwidth receivers for Very Long Baseline Interferometry (VLBI) including the broadband radio astronomy receiver presented in this article. To date, very few results

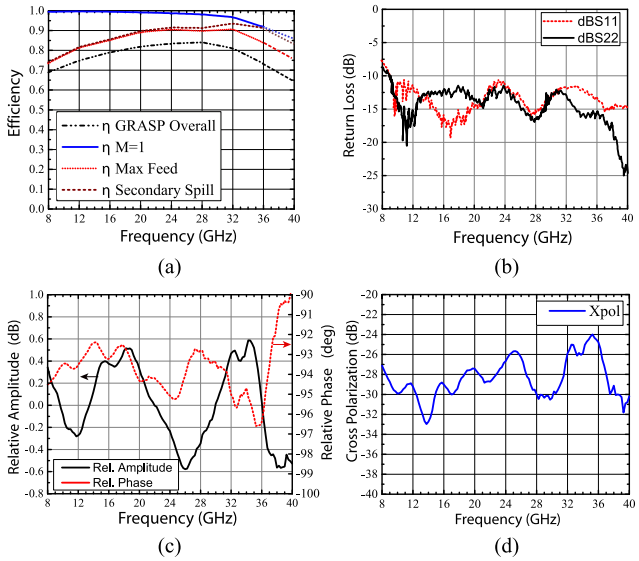

FIGURE 8. QRFH design details. (a) (GRASP) simulated aperture efficiency with the secondary focus fixed at the 32 GHz horn phase center position (36 GHz−40 GHz extrapolated). M1 is loss in power due to higher order modes, (b) Measured Return Loss, (c) Simulated Phase and Amplitude error, and d) Simulated Cross-polarization (CP) in the main lobe direction.

appear in the literature for broad bandwidth LNAs which cover the 8 GHz−40 GHz frequency range.

A. AJ50LN2N4: 4-FINGER 35 NM INP HEMT MMIC CHIP

One of the custom Monolithic Microwave Integrated Circuit (MMIC) chips developed for the ultra-wideband receiver is a 35 nm Indium-Phosphide (InP) HEMT MMIC. The AJ50LN2N4 utilizes a 4-finger gate and was fabricated by Northrop Grumman Corporation (NGC) using a 100% InAs channel. Because of its excellent very broad bandwidth performance we use this MMIC in the first low noise amplifier. The wideband LNA design consists of three stages of HEMTs separated by on-chip matching networks. The LNA builds upon HEMT MMICs designed by members of our team in [27], [29].

Common source topology was used for the 3-stage design. To achieve the broad band X- to Ka-band LNA design, we implemented a 4-finger 120 μm gate periphery transistor in the first stage, a 2-finger 50 μm gate periphery HEMT in the second stage, and a 2-finger 60 μm gate periphery HEMT in the third stage.

The HEMT model used for the design was based on a scalable 2-finger cryogenic HEMT model developed at Caltech and JPL [27]. To stabilize large 4-finger HEMTs we used additional internal airbridges within the transistor's layout to cut off internal transistor modes that can lead to oscillations as reported in [32]. The simplified schematic diagram of our LNA design is shown in Fig. 9. Microstrip lines, metal-insulator-metal capacitors, and thin-film resistors were used for inter-stage matching and bias network decoupling. Measured cryogenic (6K) performance of a measured AJ50LN2N4 4-finger 35 nm gate-length InP MMIC with an inset micrograph of the chip is shown in Fig. 10.

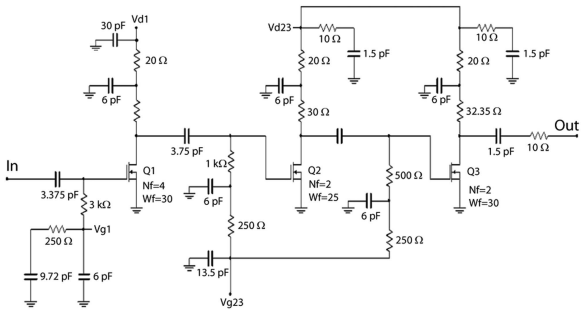

FIGURE 9. Simplified schematic of the MMIC LNA used in this work.

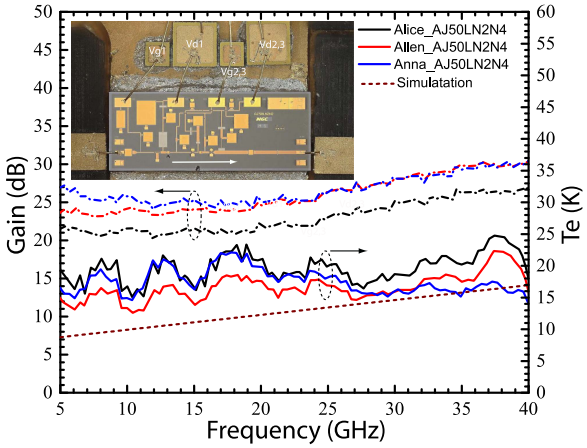

FIGURE 10. AJ50LN2N4 4-finger 35 nm InP MMIC measured effective noise temperature (TE) and derived gain. Ambient temperature was ∼6 K. The MMIC design goal was operation in the 8 GHz−50 GHz band. *Inset:* Photomicrograph of the AJ50LN4N2 NGC chip in the amplifier housing.

B. WBA850: 4-FINGER 70 NM GAAS MHEMT MMIC CHIP

We also developed [27] a second-stage LNA using OMMIC's 70 nm gate-length mHEMT MMIC fabrication process.[1] This second LNA was also designed for 8 GHz−50 GHz of bandwidth utilizing 4 finger mHEMT devices. Similarly to Fig. 10, in Fig. 11 we show the 70 nm mHEMT measured cryogenic effective noise temperature and derived gain. A micrograph of the packaged OMMIC chip is shown in 70 nm mHEMT as an inset. The associated gain ranges from 20 dB−30 dB across the band.

C. MMIC PACKAGING

The MMICs were mounted on a custom-made housing, similar to that described in [29]. The input and output of the chip are wirebonded to a 50 Ω microstrip on a 10-mil-thick CuFlon substrate [30]. This microstrip transitions to 2.9 mm connectors are inserted at the housing edges. The bias pads on the chip are wirebonded to single layer bypass capacitors to enhance stability; the DC bias network also includes surface mount capacitors and series resistors mounted on a PCB substrate that also fits inside the LNA housing. An example of the housing assembly is shown in Fig. 12.

[1] [Online]. Available: https://www.ommic.com/

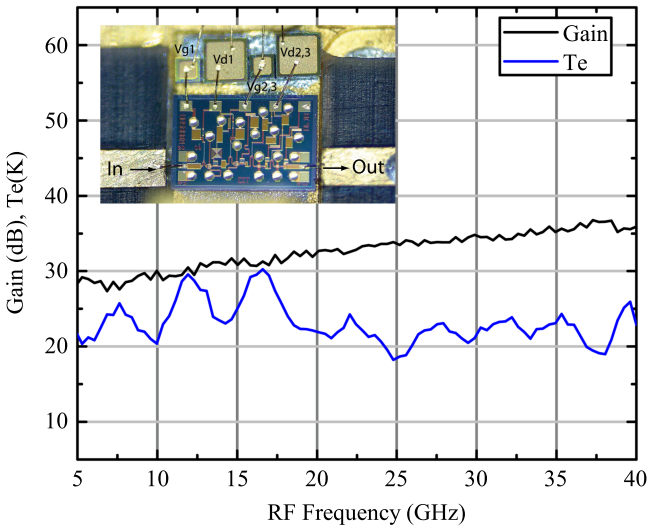

FIGURE 11. WBA850C 4-finger 70 nm OMMIC mHEMT MMIC performance (6 K). Design goal is again operation in the 8 GHz–50 GHz band. The gain increases to a frequency ≥ 40 GHz. *Inset:* Photomicrograph of the OMMIC WBA850 C mHEMT chip in an amplifier housing.

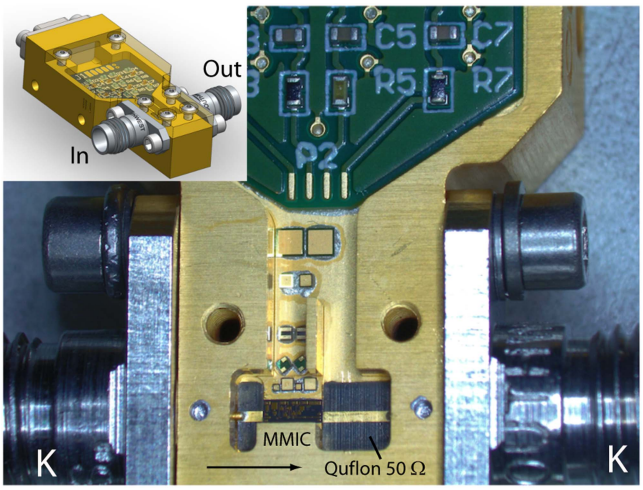

FIGURE 12. Photograph of a MMIC chip and bias PC board in a (brass) housing. The input/output connectors are 2.92 mm. *Inset:* Rendering of the low noise amplifier block.

D. CRYOGENIC PERFORMANCE OF TWO CASCADED LNA'S

We measured both individual packaged MMICs and cascaded modules in a cryostat cooled to ∼6 K in the 2020/2021 time frame. Despite significant JPL lab access challenges presented by the Covid pandamic we were able to select two chains of two MMIC LNAs in series (to minimize the noise from the first LNAs) for the X-Ka band prototype receiver (Fig. 13). The overall cryogenic gain from 8 GHz–40 GHz is between 40 dB–50 dB. The cryogenic noise over the same band varies between 13 K to 25 K. The simulated noise of the MMIC chips are approximately 5 K lower than obtained packaged. This can be explained with small errors in the noise model and additional package losses that are not accounted for, such as exact modeling of the wirebonds electric field from the MMIC to the input substrate.

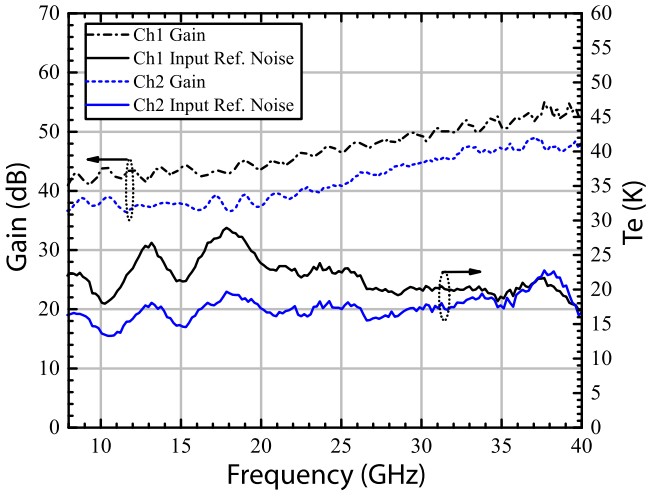

FIGURE 13. Cryogenic gain and noise of two Cascaded LNA's. The depicted curves are from the two separate packaged series LNA chains, needed for the two circular polarized receiver channels. The observed standing wave is understood to arise from a mismatch in electric field between the MMIC CPW input pads and the CuFlon [30] 50 Ω microstrip transmission line. This issue is presently under investigation and is anticipated to be addressed in a IEEE follow-on letter.

E. 35LN1A1: 4-FINGER 35 NM INP HEMT MMIC CHIP

A third LNA design with a wide bandwidth of 5 to 35 GHz in common source topology has also been developed with focus on lower noise at X-band than the prior LNAs [28]. This chip, fabricated at NGC in the same 35 nm gate-length process with 100 % indium channel content as that of Fig. 9, utilizes a 4 finger 240 μm gate periphery HEMT in the first stage, followed by two 4 finger 160 μm gate periphery HEMTs for a total of three stages.

Measurements show the packaged LNAs have a low noise temperature performance of 10 K–18 K, while operated at 10 K ambient. This result was achieved by rigorously simulating the minimum noise figure (NFmin), gain, VSWR, and stability circles across frequency for different sized HEMTs. Augmentation of the circuit model to 4-fingers was implemented by combining two 2-finger HEMT subcircuit models in parallel, similar to the method in [33]. Further adjustments were made to the augmented model by adjusting properties of the wiring interconnects within the model. This was done to better establish consistency between measured and simulated S-parameters and also of the location of the reference planes of the transistor's layout. It is noted that electrical instabilities in large 4-finger HEMTs operated at cryogenic temperatures have been observed in prior designs. The 35 nm HEMTs have high cutoff frequencies, and with cryogenic operation the mobility of electrons increases and can lead to unstable behavior if not properly compensated. To stabilize large 4-finger HEMTs we similarly used additional internal air bridges within the transistor's layout to cut off internal transistor modes that can lead to oscillations as reported by reference [32].

The measured noise and derived gain across the band are shown in Fig. 14. The inset of Fig. 14 depicts a capacitive

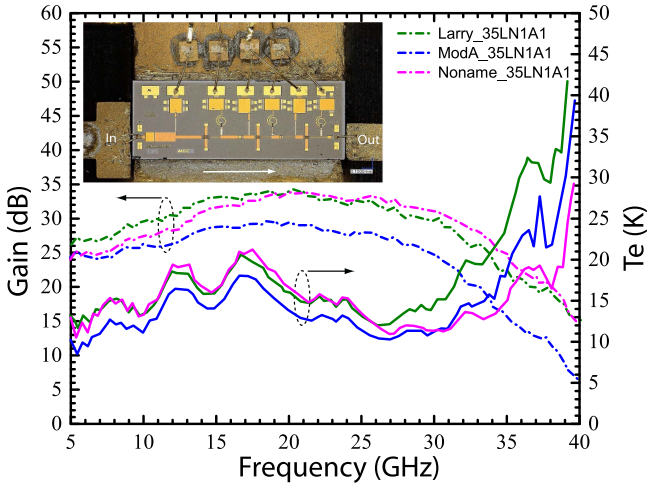

FIGURE 14. A third LNA developed for very low X-band noise is the 35LN1A1 [28]. Design goal was 5 GHz−35 GHz. Shown in the inset is a capacitive input matching section in the housing. From extensive electromagnetic simulations the bumps at 13 & 17 GHz appears due to a modal coupling mismatch which is not captured by merely assuming a 50 Ω MMIC circuit input impedance.

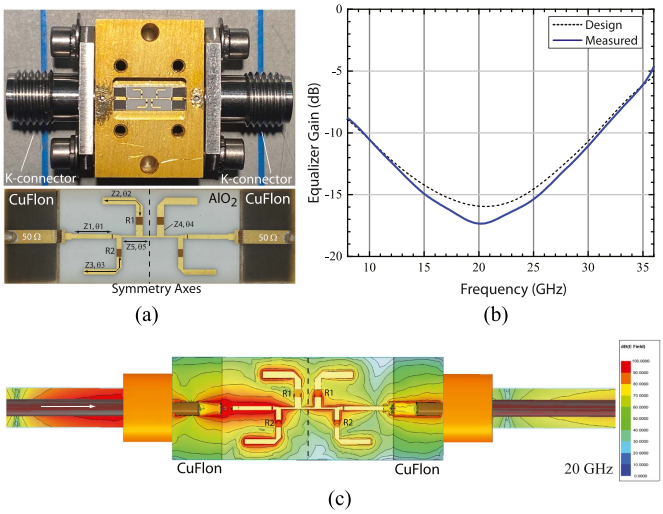

FIGURE 15. (a) Custom broadband equalizer to flatten the 35LN1A1 (Section IV-E) MMIC gain response. The equalizer is symmetric around the center line. CuFlon [30] is used as an interface dielectric to minimize parasitic reactance from the transformation of 50 Ω coax (TEM) to microstrip mode in Alumina (see text for details). (b) 8 GHz−36 GHz design (dotted) and measured (solid line) room temperature equalizer response. (c) Simulated 20 GHz Electric Field distribution. At this frequency the combined absorption/reflection loss amounts to ∼17 dB.

input matching section that is used to tune out the inductive wirebond at the MMIC input, The gain of this chip is not as flat as that for the chip in Fig. 10, however flatness of gain may be achieved using a custom-designed equalizer chip at the output of the LNA as described in the next section.

F. EQUALIZER

To equalize the gain of the 35LN1A1 (Section IV-E) we have developed a broadband equalizer covering 8 GHz−36 GHz. It is noted that in principle any shape may be compensated for. Thanks to the thin-film resistor/Alumina construction the equalizer operates with very similar performance at both room- and cryogenic temperature.

For frequencies $\gtrsim$25 GHz a broadband frequency independent RF match from the input/output coax transverse electromagnetic (TEM) mode to the Alumina substrate 50 Ω microstrip (Quasi-TEM) mode transmission line becomes increasingly difficult to achieve (dBS11 ≥ -12 dB). The reason for this is the Alumina substrate high dielectric constant ($\epsilon_r = 9.8$). Fused Quartz as an alternative substrate material has also been examined, however circuit dimensions increase with associated problems.

To mitigate the modal interface issue, we first transform to a low dielectric ($\epsilon_r = 2.05$) CuFlon [30] substrate as shown in Fig. 15(a). The 8 GHz−36 GHz em-simulated (design) and room temperature measured equalizer response is shown in Fig. 15(b). We note that the equalizer is intended to be used at room temperature after U5 in Fig. 4 in case the lower noise temperature 35LN1A1 MMIC at X-band (Section IV-E) is selected as the front end LNA (as opposed to the AJ50LN2N4 of Section IV-A). The equalizer's main electrical parameters are presented in Table 2 with Fig. 15(c) depicting the equalizer 20 GHz Electric field distribution amounting to a 'maximum' insert loss of ∼17 dB.

TABLE 2. Equalizer Electrical Dimension

Params†	Z0 (Ω)	θ (Deg)
Z1, θ1	50.0	70.6
Z2, θ2	46.2	84.6
Z3, θ3	39.1	90.0
Z4, θ4	29.0	9.25
Z5, θ5	71.3	23.5
R1	15.0	
R2	76.0	

†Ref. Fig. 15(a).

To understand the equalizer circuit behavior we depict in Fig. 16(a) the generalized functions performed by the various equalizer branch components. We start with a 50 Ω through line (red) with no frequency dependence other than ohmic circuit loss. The next function incorporated in the equalizer design is a T-arm with no thin-film series or shunt resistance (blue curve). In this case the circuit Q-factor ($\omega_r/\Delta\omega$) is finite, being set by the microstrip line ohmic loss. By adding series thin-film resistance to the through line (not T-branch) the circuit coupling efficiency is effected (purple line). And finally by adding a thin-film resistance to both the through line and T-branch we effect both the circuit performance bandwidth and coupling (green curve). Bearing in mind that the equalizer is symmetric around the center we first use a linear circuit simulator to obtain the circuit response needed to flatten the gain curve and finally an em-simulator such as HFSS [31] to come up with the final circuit (see also Fig. 15(c)). In Fig. 16(b) we show the measured gain and equivalent noise temperature from 8 GHz−36 GHz for a 35LN1A1 MMIC

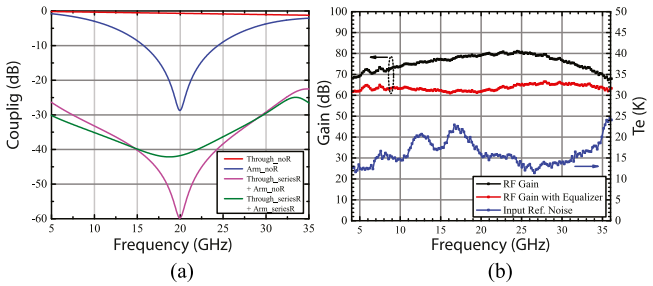

FIGURE 16. **(a) Equalizer circuit behavior of four generalized equalizer branch components. The equalizer is symmetric around the dashed horizontal line with the overall gain response an optimized circuit combination of the various branch components. See text for detail. (b) Measured 35LN1A1 RF gain with and without equalizer[2] and equivalent noise (Cascaded ∼6 K LNA configuration including RT U5 of Fig. 4).**

based LNA(U1)−Hybrid−WBA850(U2)−Miteq(U5) combination (Ref: Fig. 4).

V. FRONT-END RECEIVER SYSTEM ARCHITECTURE

In Fig. 17 we show the complete receiver front-end architecture. The quad-ridged feed and LNA development have been extensively discussed in Sections III & IV. In this section we focus on the remaining front-end hardware and physical implementation. As seen from Fig. 17(a) the QRFH, cooled LNA's and quadrature hybrid are build around a Sumitomo two stage Gifford-McMahon (GM) cycle RDK-205D 4 K coldhead [25]. The first-stage operating temperature is ∼37 K with the second stage coldhead at ∼3.5 K. Under normal bias conditions the LNA ambient temperature is between 5.3 K−5.5 K. Inside the vacuum space the feed is ridged (Section III) whereas outside the vacuum vessel the feed is conical in shape. This structure facilitates the 300 K pressure window interface.

Natively the feed output is linearly polarized which is translated to right and left hand circular polarization by means of a 8 GHz−40 GHz quadrature hybrid (next section). Fig. 17(b) and (c) show the cascaded LNA−90° Hybrid−LNA two channel setup. The hybrid serves to direct reflected noise waves from the second amplifier to a 50 Ohm termination providing ≳15 dB isolation between the cascaded amplifier stages, thereby significantly reducing standing inter-module standing waves. In this configuration the hybrid serves as substitute for a "non-existing" cryogenic broadband isolator. In front of the first LNA a 20 dB directional coupler driven by a 6 dB cold attenuator facilitates injection of either a tone or calibrated noise. This signal path was used in Section VII-D for measuring the receiver phase stability.

A. 8 GHZ–40 GHZ QUADRATURE HYBRID

In collaboration with Yebes Observatory (Spain), a custom 8 GHz−40 GHz cryogenic quadrature hybrid has been developed (Fig. 18). This is a key component in the receiver system since it allows: *1)* to convert the QRFH linear polarization output into circular polarization, *2)* the cascading of two LNAs as discussed in section IV, and *3)* the combining of two LNAs to form a balanced amplifier (not discussed in this paper), greatly improving return loss of the single ended units and reducing the sensitivity to the input mismatch. It is important in all this to keep the insertion loss of the hybrid as low as possible to avoid adding excessive noise to the receiver system.

The hybrid is designed with offset broadside coupled lines in stripline technology using a structure similar to the one

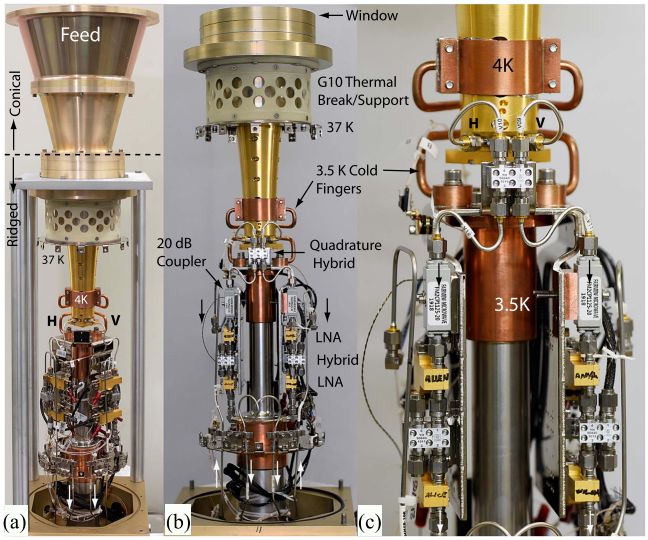

FIGURE 17. **(a) The Front-end receiver architecture. Shown are the feedhorn, vacuum break, cascaded LNA assembly, and cryostat cold head [25]. (b), (c) Progressively zoomed in photographs. See text for detail.**

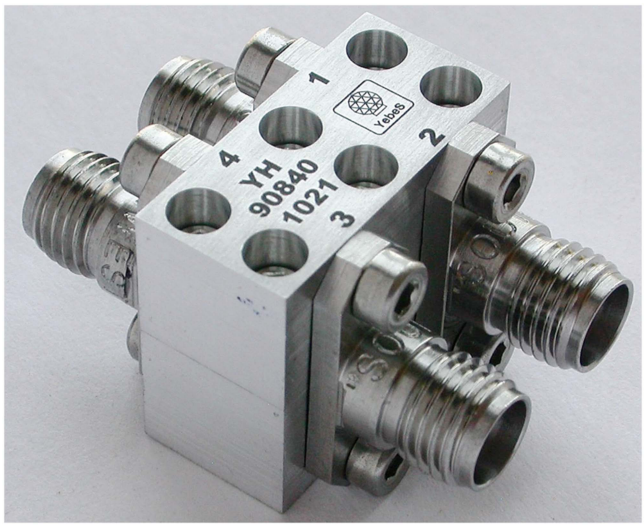

FIGURE 18. **Yebes Observatory 8 GHz–40 GHz cryogenic quadrature hybrid. The total dimensions of the unit without connectors are 19 x 9 x 16.1 mm.**

[2]35LN1A1(U1)−Hybrid−WBA850(U2)−Miteq(U5) Combination

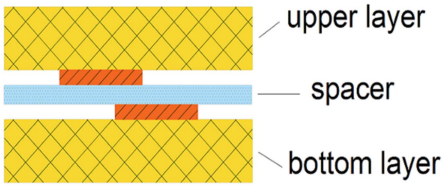

FIGURE 19. Schematic representation of the hybrid layer structure. The high coupling is achieved using offset broadside coupled lines separated by a thin dielectric. The offset allows a fine tuning of their coupling.

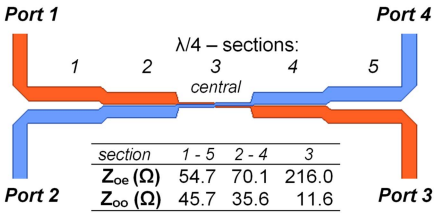

section	1 - 5	2 - 4	3
Z_{oe} (Ω)	54.7	70.1	216.0
Z_{oo} (Ω)	45.7	35.6	11.6

FIGURE 20. Schematic of the top-view of the geometry of the five λ/4-section coupled lines. The bottom table presents the even and odd impedances of each λ/4-section.

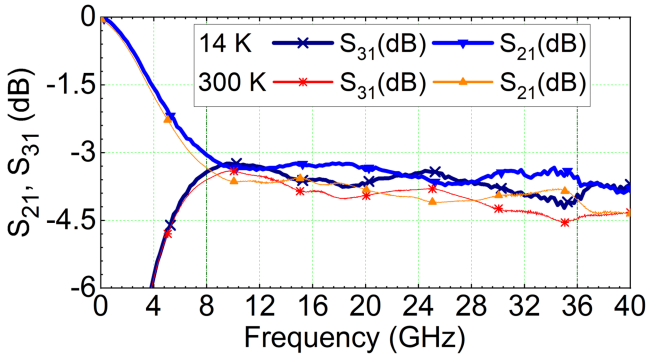

FIGURE 21. Measured transmission performance at 300 K and 14 K temperature. Almost no degradation in performance is observed when cooled down except for the expected reduction of the dissipative loss.

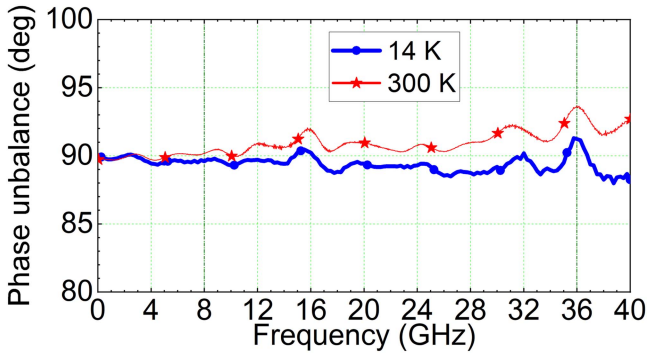

FIGURE 22. Measured phase at 300 K and 14 K temperature between 0 GHz–40 GHz. The $\delta\theta$ is $\leq \pm 1.8°$ across the most of the band. It is surmised that the peaks at 16-, 32-, 36 GHz are due to constructive interference from internal standing waves.

described in [34] consisting of a stack of three layers: The bottom substrate-line layer, a dielectric spacer and the upper line-substrate layer, all of them enclosed in a metal box (see Fig. 19). The requirement of a large 5:1 fractional bandwidth with a low amplitude and phase ripple in the band has been achieved using five sections of λ/4 coupled lines, as can be seen in Fig. 20. The symmetry of the structure in X and Y axes (with sections 1 and 5 equal to each other as well as sections 2 and 4) keeps isolation in values comparable to the return loss. The large coupling required in the central λ/4 section was obtained by using a very thin 6 μm dielectric spacer. The software tool used for the simulation was Keysight Momentum [35].

The performance of the hybrid is very sensitive to the accuracy of the dimensions of the central section (on the order of few tens of microns for the width of the lines and the offset between them), so an extremely careful manufacturing and alignment of the upper and bottom substrates is required. To achieve this, the process of etching and cutting the substrates was performed in the same operation with a precision laser milling machine.[3]

The hybrid must operate at temperatures lower than 15 K without degradation. The materials have been selected not only by their thermal stability but also to match their expansion coefficients in the z axis. This means that they will shrink approximately by the same amount so the performance of the hybrid will remain almost unchanged when cooled down. The substrates used for the bottom and upper layers are RT/duroid 6002 [36] Electrodeposited Copper Foil 10 mils thick, the spacer is Mylar and the box is machined out of 6082 aluminum.

The reliability of the contact between the lines and the input/output connectors is a very important practical problem. The mechanical stress produced by the variation between the ambient and the cryogenic temperature, can easily lead to failures in the solder joints after repeated thermal cycles. To minimize this risk, we have used connectors with a sliding central pin made by Southwest Microwave [37] which allows slight shifts of the central pin alleviating the mechanical stress. The pins were glued with H20E conductive epoxy [38] to the circuit lines. Finally, a careful design of the connector to the stripline- transition has been performed in order to improve the return loss.

The results obtained are presented in Figs. 21–23 and Table 3. From those it is clear that the effect of cooling is reducing the loss as expected while the coupling and the reflection remain almost constant. S parameters were measured in a 14 K cryostat system. The S-parameter calibration was performed at ambient temperature requiring a small correction for the variation of losses in stainless steel thermal transitions

[3]Protolaser 200 from LPKF Laser & Electronics.

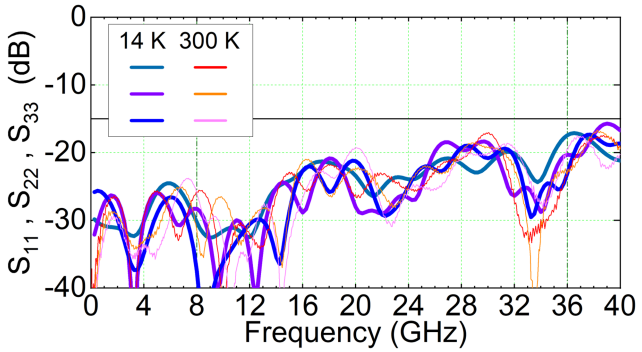

FIGURE 23. Four port measured input return loss at both 300 K and 14 K between 0 GHz–40 GHz. The return loss is ≤18 dB across the most of the band, explaining the effectiveness of significantly reducing front-end cascaded LNA inter-module standing waves (Fig. 17).

TABLE 3. 8 GHz–40 GHz Cryogenic Hybrid

Serial Number	YH90840	
Description	90° Cryogenic Hybrid	
Nominal Coupling	3 dB	
Connector	2.92 mm sliding pin	
Frequency Band	8 GHz – 40 GHz	
Temperature	**14 K**	**300 K**
Return Loss dB (Max. any port)	16	16
(90 % bandwidth)	(17)	(17)
Amplitude Unbalance (dB) (max.)	0.35	0.36
Phase Unbalance (deg) (max.)	2	4
A. E. Insertion Loss dB (max.)	0.76	1.24
Isolation (dB) (min.)	17	17

and semi rigid connecting coaxial cable at cryogenic temperature, in a similar way as was done in [39]. Time domain gating was also used to avoid the effect of small changes of the input and output access lines when cooled.

VI. IF PROCESSOR

Following the front-end ∼40 dB cold gain RF amplification is a room temperature IF processor / down-converter which subdivides the X, (K), Ka bands into four 4 GHz–8 GHz IF channels (for both right- and left hand circular polarization). In principle it is also possible to process the Ku (12 GHz–18 GHz) bands, thereby acquiring four dual polarized microwave bands with one receiver. However at the present time this is beyond the scope of the research task.

Fig. 24 depicts the breadboard IF processor, following the circuit block diagram of Fig. 4. For the planned prototype receiver test observations at the Owens Valley VLBA antenna we have substituted the Ka-band bandpass filter (BPF2) with a K-band BPF (BPF3). In Table 4 we compile a listing of the most relevant components used in the cryogenic RF front-end and IF processor/down-converter system.

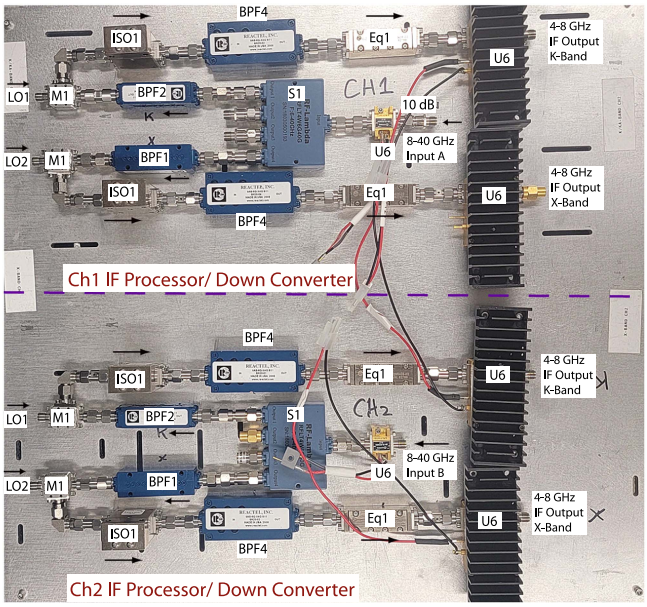

FIGURE 24. X & Ka band breadboard IF processor and down-converter. Referring to Table 4, for the VLBA observations BPF2 has been replaced with BPF3 everything else being the same.

TABLE 4. X-Ka Band Rx Component List

Desig.	Manufacturer	P/N	Notes
H1	Yebes	H8_40	Section V-A
C1	Fairview	FM2CP1125-20	20 dB Coupler
U1	NGC/JPL	AJ50L2N4	LNA, Section IV-A
U2	NGC/JPL	WBA850	LNA, Section IV-B
U3	NGC/JPL	AJ50L2N4	LNA, Section IV-A
U4	NGC/JPL	AJ50L2N4	LNA, Section IV-A
U5	Miteq	LNA-20-00104000-58-5P	0.1-40 GHz, 25 dB
U6	RF Lambda	RLNA01G12GA	2-10 GHz Driver
S1	RF Lambda	RFLT4W6G40G	4 way Power splitter
BPF1	Reactel	9AS-10G-X4GS11	8-12 GHz BPF
BPF2	Reactel	9AS-31G-X10GK11	27-36 GHz BPF
BPF3	Reactel	8CX11-22.5G-X9GK11	18-27 GHz BPF
BPF4	Reactel	9AS-6G-X4GS11	4-8 GHz BPF
M1	Marki	MM1-0832LS	8-32 GHz Bal. Mixer
M2	Marki	MM1-1044LS	9-44 GHz Bal. Mixer
Iso1	Fairview	FMIR1006	4-8 GHz Isolator
Eq1	Eclipse	EQN0408-03	3 dB Equalizer
Eq2	Custom	8-36 GHz	Section IV-F

VII. SYSTEM PERFORMANCE

A. RECEIVER NOISE PERFORMANCE

As opposed to the LNA equivalent temperature of Section IV, adding in a real receiver system the QRFH, 50 μm vacuum pressure window, quadrature hybrid, directional coupler, and interconnecting phase matched coax cables in front of the first LNA inevitably increase the (SSB) receiver noise temperature. Every effort, including operating at ∼5.4 K ambient temperature [25], has been made to minimize the additive thermal noise of the aforementioned front-end components.

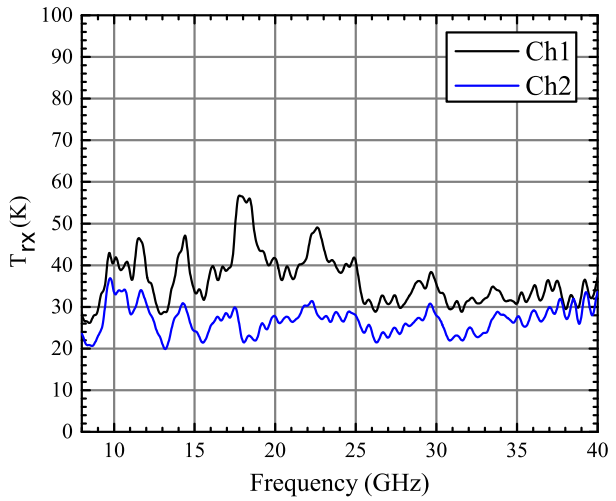

FIGURE 25. "On sky" (SSB) measured system noise temperature of the two circular polarized receiver channels. Because of the Covid pandemic lab access in 2020/2021 was very difficult and as a result channel 1 was not optimized and thus presents a "worst case" scenario. See text for details.

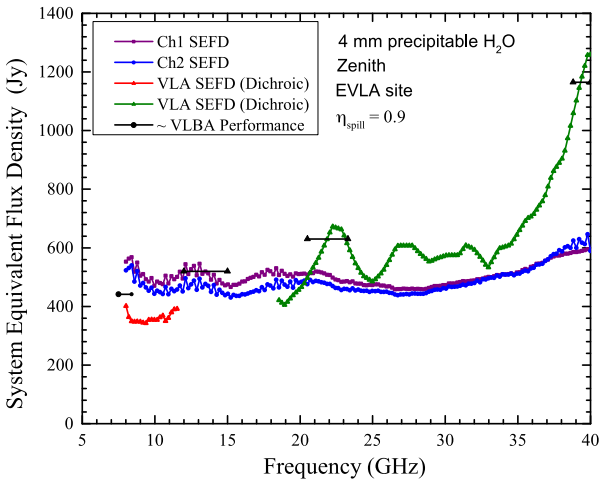

FIGURE 26. Comparison of the (derived) system equivalent flux density (SEFD) of the JPL X–Ka band protoytype receiver vs. existing receiver performance at the New Mexico very large array (VLA) and the VLBA [40]. Performance is very competitive for the 5:1 frequency range receiver except for X-band. As discussed in Section IV-E, the 5 GHz–35 GHz 35LN1A1 MMIC LNA may be used as the first amplifier if this of concern. Note the in principle continuous frequency coverage.

TABLE 5. Ch2 Receiver Noise Budget

Noise (K)	8 – 12[†]	12 – 18	18 – 27	26.5 – 40
Conical Feed	0.9	0.9	0.9	0.9
Window / Spill[‡]	8.7	6	5.5	5.5
QRFH to Hybrid	0.25	0.25	0.25	0.25
Horn Reflection	0.6	0.35	0.35	0.35
Coax (10 cm)	0.4	0.45	0.6	0.8
Hybrid	0.35	0.4	0.5	.65
20 dB Coupler	0.65	0.65	0.65	0.65
LNA	15 ± 1	16 ± 1	17.5 ± 1	19 ± 2
T_{rx} (K)	27 ± 6	25 ± 5	26 ± 4	28 ± 3

[†]GHz
[‡]50 μm Kapton pressure window

The "on-the-sky" receiver noise temperature (T_{rx}) for the two circular polarized receiver channels is shown in Fig. 25.

Development and system integration of the LNA modules occurred in 2020/2021 during the height of the Covid pandemic with very limited, and on occasion no, laboratory access. Receiver channel 2 represents the noise performance that can be achieved with a set of optimized LNA modules whereas channel 1 suffered from very limited work space access. Importantly, the measured results of Fig. 25 infer the variance in receiver sensitivity performance between an optimized and non-optimized LNA system. Thus in production adequate time should be devoted to down-select optimized low noise front-end LNA's with suitably matched back-end LNA's operating well in unison. In Table 5 we provide a system noise budget based on the receiver channel 2. The observed standard deviation (σT_{rx}) is understood to be due to constructive, or deconstruction, interference of standing waves between the various RF components.

B. RECEIVER SEFD

To obtain a sense of comparison with the VBLA sensitivity in the X–Ka band we have translated the measured receiver noise temperature of Section VII-A to a system equivalent flux density (SEFD) (Jy), where the SEFD is defined as the flux density of a radio source that doubles the system temperature [40]. To do so we first calculate the added sky noise via an atmospheric model obtained optical depth (τ) for a 4 mm precipitable (in zenith) water column, an average value at the New Mexico VLA site.

$$T_{sky} = T_{atm}(1 - \eta_{spill} \cdot \eta_{atm}) \tag{1}$$

with

$$\eta_{atm} = e^{-\tau}. \tag{2}$$

Here $T_{atm} = 0.95 T_{sky}$ (290 K) and the assumed spillover efficiency (η_{spill}) 0.9. For the VLA 25–meter paraboloid antennas the SEFD is given by the equation SEFD $= 5.62\ T_{sys}/\eta_A$, where we have used for the aperture efficiency 'η GRASP Overall' of Fig. 8(a) for η_A. T_{sys} is obtained from

$$T_{sys} = \frac{T_{rx} + T_{sky}}{\eta_{atm}}. \tag{3}$$

In Fig. 26 we compare the JPL prototype X-Ka band receiver with documented VLA SEFD's using a room temperature dichroic filter for dual frequency observation in S & X band. We see that the presented sensitivity performance of Fig. 25 is very competitive at RF frequencies above ~15 GHz. In X-band (8 GHz–12 GHz) the VLBA sensitivity is slightly better, however this situation has been addressed in Section IV-E where if so desired the 50 GHz AJ50LN2N4 MMIC based first LNA maybe substituted for a 35 GHz 35LN1A1 MMIC chip design.

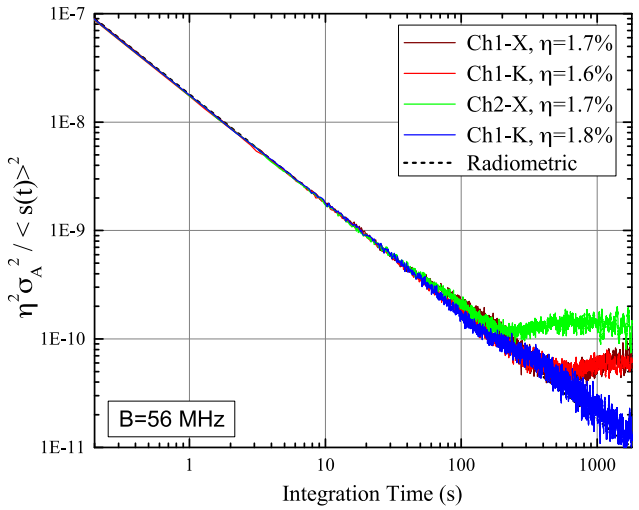

FIGURE 27. Normalized differential "end-to-end" Allan Variance system stability for X & K band in both RCP and LCP. Data was taken at 5 GHz and 7 GHz in a 56 MHz IF passband giving a differential Allan time ≥ 200 s. An actual digital spectrometer will have the channels much closer spaced than the analog filter bank 2 GHz spacing used in this lab setup measurement, thus providing a much higher degree of common mode noise rejection and subsequent differential Allan Variance system stability time. Data was taken in a 12 h period overnight for each of the four channels.

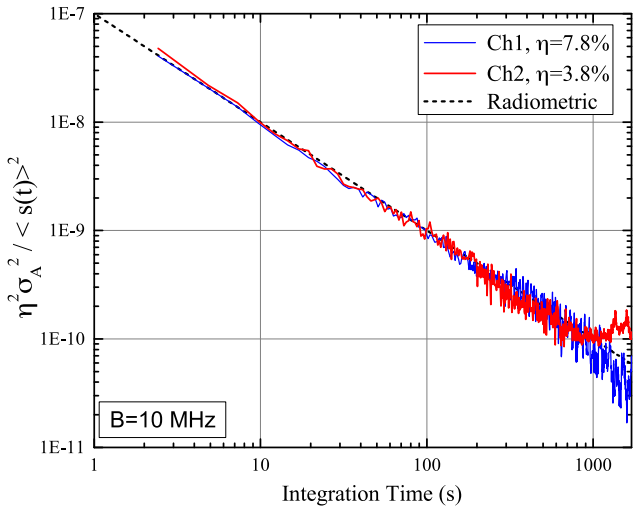

FIGURE 28. Normalized Allan Variance phase measurement of a 30 GHz injected tone (See text for detail.). The phase stability appears to be ≥1000 s.

C. DIFFERENTIAL AMPLITUDE STABILITY

In general, receiver instabilities lead to a loss in integration efficiency and poor baseline subtraction. Throughout the X−Ka receiver design process careful attention has been given to the multiplicity of factors that have the potential to degrade the receiver stability [41], [42]. To characterize the instrument system (continuum and differential) stability the X- and K band IF outputs (4) were send through two (analog) 56 MHz bandpass filters [21] centered on 5 GHz and 7 GHz. As back-end processor we used two Herotek DT4080 tunnel diode detectors [43] connected to a NI USB-6343 [44] data acquisition system.

The two channel IF system enables us to take measurements of the (continuum) Allan variance [45], [46] in two single IF bins simultaneously. By removing the IF signal common mode as in

$$s(t') = \frac{1}{\sqrt{2}}\left[\left(\frac{x_i(t')}{\langle x\rangle} - \frac{y_i(t')}{\langle y\rangle}\right)+1\right]\cdot\frac{\langle x\rangle + \langle y\rangle}{2}, \qquad (4)$$

with $x(t')$ and $y(t')$ the original measurements of the powers in each IF channel as a function of time t' the differential Allan system stability response may be calculated (Fig. 27). It is noted that is is the differential stability we are interested in as the instrument will be used in an interferometric (multi-beam) network. Data was taken overnight for each of the four channels. To match the radiometer equation [47] we derive an effective data acquisition rate of ∼1.7%.

D. PHASE STABILITY

To obtain a measure of the instrument phase stability we connected a Keysight UXA Signal Analyzer (N9040B) between the receiver noise injection port and IF output (Fig. 4). By injecting a 30 GHz CW tone and monitoring S21 we were able to extract the instrument dθ(t) time series in Ka-band. Taking the Alan variance [45] on the thus obtained 30 GHz tone temporal phase stability provides an Alan stability time in excess of 1000 s, as shown in Fig. 28.

VIII. VLBA PROTOTYPE RECEIVER INSTALLATION

In July 2022 the 8 GHz–40 GHz prototype receiver was taken to the Owens Valley VLBA antenna for installation (Fig. 29). The receiver is mounted in a spare slot in the VLBA receiver cabin, being straddled between the 4 cm (8.4 GHz) and 13 cm (23 GHz) VLBA single band receivers. The VLBA dual-shaped 25 m Cassegrain Antenna utilizes a 7.93° extended angle ring focus [22] to illuminate the individual feedhorns, as depicted in Fig. 29 inset.

Referring to Fig. 4, the local oscillator signal needed to down-convert the "on-the-sky' RF signal into the 4 GHz–8 GHz IF passband is 16 GHz for X-band (LSB-IF), 14 GHz–19 GHz for K-band (USB-IF), and 23 GHz–28 GHz for Ka-band (LSB-IF). In the case of the Owens Valley VLBA operation we interface to one of the observatory's synthesizers set to 15.8000 GHz, thus observing 7.8 GHz–11.8 GHz (LSB-X) and 19.8 GHz–23.8 GHz (USB-K).

On 25 Aug 2022 after installation of the down-converter/IF processor of Fig. 24 and the LO/bias hardware, but prior to cooling the receiver, we were able to obtain the preliminary "on sky" 22.235 GHz waterline test spectrum of Fig. 30. The observation were taken simultaneously in X & K-band under the following conditions: Surface temperature 40 °C, surface pressure 880 mbar, relative humidity 40%, altitude 1.2 km. Data was taken on a Keysight Model N9917 A spectrum analyzer. The room temperature SSB receiver system noise temperatures were 546 K in X- and 628 K in K-band. This includes thermal noise from the 40 °C Kapton feedhorn window

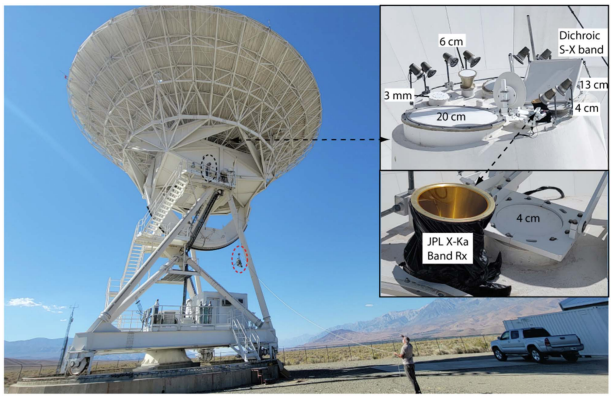

FIGURE 29. Installation of the 8 GHz−40 GHz wideband receiver at the Owens valley VLBA antenna. Shown is the receiver being hoisted up to the Apex room with the assistance of Jim Brown (NRAO) and Hamid Javadi (JPL). *Inset:* The reference frame prototype receiver feedhorn protruding out of the receiver cabin. 50 μm Kapton is used to protect the feed from weather.

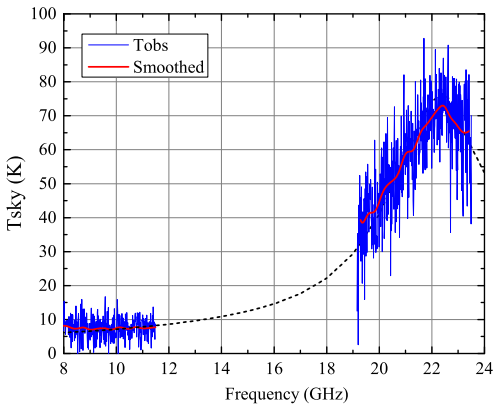

FIGURE 30. 22.325 GHz simultaneous X- & K-band water line observation in Zenith in on 25 Aug 2022 with the 8 GHz−40 GHz wideband receiver uncooled. The dotted line is modeled sky brightness temperature and fits the data well. See text for detail.

(radome), 25 °C QRFH, vacuum window, Yebes quadrature hyrbid, interconnecting coax lines, and 20 dB directional coupler. Correcting for the room temperature incurred front-end loss(es), the receiver noise temperature is as what would be expected with the RF LNA's being at room temperature.

IX. CONCLUSION

Until fairly recent the majority of AGN centered imaging was accomplished in the S (2.3 GHz) and X (8.4 GHz) radio frequency bands, however S-band observations for reasons such as sensitivity "plateauing", increased source structure (jets), and radio frequency interference (RFI) have become less rewarding. To circumvent these issues, and support next generation (ICRF-3) VLBI reference frame observations of extra-galactic distant AGNs, has motivated the development of an ultra-wideband X−Ka band (8 GHz−40 GHz) "Radio Astronomy" receiver.

The acquisition of data in the 8 GHz−40 GHz range consolidates several receiver systems (X, Ku, K, and Ka) into one receiver package, saving space, power, minimizes complexity, and maintenance cost. In addition to Astrometry and Geodesy, measurements of simultaneous X and Ka band allows for calibrations of both the Earth's ionosphere and solar plasma at the exact time and direction of the observations. The ultra broadband receiver also has direct application to the field of Astronomy.

The goal of this receiver is to achieve less than a 20% increase in noise over the Jansky Very Large Array (JVLA, NRAO) performance specification, which in such a wide bandwidth represents a revolutionary capability (Fig. 26). To achieve this goal a number of key technologies, such as: 1) a 5:1 frequency ratio ultra wideband dual polarization feedhorn (compatible with VLBA optics), 2) low noise 8 GHz−50 GHz cryogenic MMIC amplifiers, 3) a $2^1/_2$ octave wide 8 GHz−40 GHz cryogenic quadrature hybrid, 4) a custom shaped 8 GHz−36 GHz equalizer, and 5) a quad-band IF Processor / down-converter to a common 4 GHz−8 GHz IF, have been developed. The wideband receiver is presently installed at the Owens Valley VLBA antenna for on the sky system performance evaluation.

ACKNOWLEDGMENT

The authors gratefully acknowledge the National Radio Astronomy Observatory for facilitating access to the Owens Valley (OV) VLBA antenna for test observations, Dr. Jay Blanchard for managing the OV VLBA Project on NRAO's side, William Martin of NRAO for advice and mechanical calculation support, and Jim Brown for all his assistance and enthusiasm installing the 8 GHz−40 GHz receiver at the Owens Valley VLBA Antenna. We also thank Dr. Walter Brisken of NRAO for his very helpful support and advice and finally Stephen Montanez of JPL for the careful assembly of the LNA blocks. The research described herein was carried out at the Jet Propulsion Laboratory, California Institute of Technology, USA, under contract with the National Aeronautics and Space Administration. Copyright 2022. All rights reserved.

REFERENCES

[1] A. de Witt, P. Charlot, D. Gordon, and C. Jacobs, "Overview and status of the international celestial reference frame as realized by VLBI," *Universe*, vol. 8, no. 7, 2022, Art. no. 374, doi: 10.3390/universe8070374.

[2] R. S. Park, W. M. Folkner, J. G. Williams, and D. H. Boggs, "The JPL planetary and lunar ephemerides DE440 and DE441," *Astronomical J.*, vol. 161, no. 3, 2021, Art. no. 165, doi: 10.3847/1538-3881/abd414.

[3] E. F. Arias, P. Charlot, M. Feissel, and J. F. Lestrade, "The extragalactic reference system of the International Earth Rotation Service, ICR," *Astron. Astrophys.*, vol. 303, pp. 604–608, 1995.

[4] M. J. Reid et al., "Trigonometric parallaxes of high-mass star-forming regions: Our view of the milky way," *Astrophys. J.*, vol. 885, no. 2, 2019, Art. no. 131, doi: 10.3847/1538-4357/ab4a11.

[5] A. J. Beasley and J. E. Conway, "VLBI phase referencing. Very long baseline interferometry and the VLBA," in *Proc. Astronomical Soc. Pacific Conf. Ser.*, J. A. Zensus and P. J. Diamond Napier, Eds., vol. 82, 1995, Art. no. 327. [Online]. Available: https://articles.adsabs.harvard.edu/pdf/1995ASPC...82..327B

[6] E. Fomalont, S. Kopeikin, C. Lanyi, and J. Benson, "Progress in measurements of the gravitational bending of radio waves using the VLBA," *Astronomical J.*, vol. 699, pp. 1395–1402, 2009, doi: 10.1088/0004-637X/699/2/1395.
[7] H. Hellmers, S. Bachmann, D. Thaller, M. Bloßfeld, and M. Seitz, "Combined IVS contribution to the ITRF2020, EGU general assembly 2021," EGU 21–10678, Apr. 19–30, 2021, doi: 10.5194/egusphere-egu21-10678.
[8] T. M. Eubanks, "Variations in the orientation of the earth," in *Contributions of Space Geodesy to Geodynamics: Earth Dyn.* (Geodynamic Series), vol. 24, D. E. Smith and D. L. Turcotte, Eds. Washington, DC, USA: Amer. Geophysical Union, 1993, no. 1, pp. 1–54. [Online]. Available: https://agupubs.onlinelibrary.wiley.com/doi/pdf/10.1029/GD024
[9] M. Feissel-Vernier, "Selecting stable extragalactic compact radio sources from the permanent astrogeodetic VLBI program," *Astron. Astrophys.*, vol. 403, no. 1, pp. 105–110, May 2003, doi: 10.1051/0004-6361:20030348.
[10] A. Moór, S. Frey, S. B. Lambert, O. A. Titov, and J. Bakos, "On the connection of the apparent proper motion and the VLBI structure of compact radio sources," *Astronomical J.*, vol. 141, no. 6, pp. 178–186, Jun. 2011, doi: 10.1088/0004-6256/141/6/178.
[11] O. Titov, S. B. Lambert, and A.-M. Gontier, "VLBI measurement of the secular aberration drift," *Astron. Astrophys.*, vol. 529, p. A91, May 2011, doi: 10.1051/0004-6361/201015718.
[12] L. Hunt, A. de Witt, D. Gordon, C. S. Jacobs, and A. de Witt, "Comparing images of ICRF sources at S, X., K. and Q-bands," in *Proc. 12th IVS Gen. Meeting*, Helsinki, Finland (virtual), 2022. [Online]. Available: https://ivscc.gsfc.nasa.gov/publications/gm2022/57_hunt_etal.pdf
[13] D. Gordon, "Impact of the VLBA on reference frames and earth orientation studies," *J. Geodesy*, vol. 91, pp. 735–742, 2017, doi: 10.1007/s00190-016-0955-0.
[14] P. Charlot et al., "The third realization of the International Celestial Reference Frame by very long baseline interferometry," *Astron. Astrophys.*, vol. 644, 2020, Art. no. A159, doi: 10.1051/0004-6361/202038368.
[15] D. Gordon, A. deWitt, and C. S. Jacobs, "Position and Proper Motion of Sagittarius A* in the ICRF3 Frame from VLBA Absolute Astrometry," *Astron. Astrophys.*, vol. 165, no. 2, Feb. 2023, doi: 10.3847/1538-3881/aca65b.
[16] O. J. Sovers, J. L. Fanselow, and C. S. Jacobs, "Astrometry and geodesy with radio interferometry: Experiments, models, results," *Rev. Modern Phys.*, vol. 70, no. 4, pp. 1393–1454, Oct. 1998, doi: 10.1103/RevModPhys.70.1393.
[17] L. Spitzer, *Physics of Fully Ionized Gases*. 2nd Ed., New York, NY, USA: Interscience Publishers ING, 1962, Art. no. 170.
[18] Yebes Observatory Spain. [Online]. Available: https://astronomia.ign.es/web/guest/icts-Yebes/acercade
[19] A. Akgiray, "New technologies driving decade-bandwidth radio astronomy: Quad-ridged flared horn & compound-semiconductor LNAs, caltech," Ph.D. dissertation, California Inst. Technol., Pasadena, CA, USA, 2013. [Online]. Available: https://thesis.library.caltech.edu/7644/
[20] J. Yang, J. Flygare, M. Pantaleev, and B. Billade, "Development of quadruple-ridge flared horn with spline-defined profile for band B of the Wide Band Single Pixel Feed (WBSPF) advanced instrumentation programme for SKA," in *Proc. IEEE Int. Symp. Antennas Propag.*, 2016, pp. 1345–1346, doi: 10.1109/APS.2016.7696380.
[21] Reactel Inc. [Online]. Available: https://reactel.com/
[22] P. J. Napier, "The VLBA design," in *Proc. VLBI VLBA, ASP Conf. Ser.*, 1995, vol. 82. [Online]. Available: https://www.aspbooks.org/publications/82/59.pdf
[23] "CST studio suite | electromagnetic field simulation software," [Online]. Available: https://CST.com/
[24] "TICRA GRASP | antenna and EM modeling software," [Online]. Available: https://www.ticra.com/software/grasp/
[25] "Shi Cryogenics Group," [Online]. Available: http://www.shicryogenics.com/products/cryocoolers/two-stage-gifford-mcmahon-cryocoolers/
[26] "NRAO," [Online]. Available: https://public.nrao.edu/ngvla/
[27] A. H. Akgiray et al., "Noise measurements of discrete HEMT transistors and application to wideband very low-noise amplifiers," *IEEE Trans. Microw. Theory Techn.*, vol. 61, no. 9, pp. 3285–3297, Sep. 2013, doi: 10.1109/TMTT.2013.2273757.
[28] A. Fung et al., "X- to Ka- band cryogenic LNA module for very long baseline interferometry," in *Proc. IEEE/MTT-S Int. Microw. Symp.*, 2020, pp. 189–192, doi: 10.1109/IMS30576.2020.9224106.
[29] J. E. Velazco et al., "Ultra-wideband low noise amplifiers for the next generation very large array," in *Proc. IEEE Aerosp. Conf.*, 2019, pp. 1–6, doi: 10.1109/AERO.2019.8742126.
[30] Crane Aerospace & Electronics. [Online]. Available: https://www.craneae.com/sites/default/files/documents/DS_CuFlon_04122021.pdf
[31] "Ansys HFSS | 3D high frequency simulation software," [Online]. Available: https://www.ansys.com
[32] G. Moschetti et al., "Stability investigation of large gate-width metamorphic high electron-mobility transistors at cryogenic temperature," *IEEE Trans. Microw. Theory Techn.*, vol. 64, no. 10, pp. 3139–3150, Oct. 2016, doi: 10.1109/TMTT.2016.2598168.
[33] M. Varonen et al., "An MMIC low-noise amplifier design technique," *IEEE Trans. Microw. Theory Techn.*, vol. 64, no. 3, pp. 826–835, Mar. 2016, doi: 10.1109/TMTT.2016.2521650.
[34] I. Malo-Gómez, J. D. Gallego-Puyol, C. Diez-Gonzalez, I. López-Fernádez, and C. Briso-Rodriguez, "Cryogenic hybrid coupler for ultra-low-noise radio astronomy balanced amplifiers," *IEEE Trans. Microw. Theory Techn.*, vol. 57, no. 12, pp. 3239–3245, Dec. 2009, doi: 10.1109/TMTT.2009.2033874.
[35] "Keysight | advanced design system (ADS)," [Online]. Available: https://www.keysight.com/us/en/products/software/pathwave-design-software/pathwave-advanced-design-system.html
[36] "Rogers corporation advanced circuit materials division," [Online]. Available: https://www.rogerscorp.com/
[37] "Southwest Microwave 1014-01SF, 2.92 mm K-connector," [Online]. Available: https://mpd.southwestmicrowave.com/
[38] Epoxy Technology Inc. [Online]. Available: https://www.epotek.com/
[39] J. D. Gallego, I. López-Fernández, and C. Diez, "A measurement test set for ALMA band 9 amplifiers," in *Proc. 1st Radionet Eng. Forum Workshop*, 2009, pp. 23–24.
[40] NRAO. [Online]. Available: https://science.nrao.edu/facilities/vla/docs/manuals/oss/performance/sensitivity
[41] J. W. Kooi, G. Chattopadhyay, M. Thielman, T. G. Phillips, and R. Schieder, "Noise stability of SIS receivers," *Int J. Infrared Millimeter Waves*, vol. 21, no. 5, pp. 689–716, May 2000. [Online]. Available: https://link.springer.com/article/10.1023/A:1026452324545
[42] J. W. Kooi et al., "Stability of heterodyne terahertz receivers," *J. Appl. Phys.*, vol. 100, Sep. 2006, Art. no. 064904, doi: 10.1063/1.2336498.
[43] Herotek Inc. [Online]. Available: http://www.herotek.com/
[44] NI. [Online]. Available: https://www.ni.com/en-us/support/model.usb-6343.html
[45] R. Schieder and C. Kramer, "Optimization of heterodyne observations using allan variance measurements," *Astron. Astrophys.*, vol. 373, pp. 746–756, Jul. 2001, doi: 10.1051/0004-6361:20010611.
[46] V. Ossenkopf, "The stability of spectroscopic instruments: A unified Allan variance computation scheme," *Astron. Astrophys.*, vol. 479, pp. 915–926, Mar. 2008, doi: 10.1051/0004-6361:20079188.
[47] J. D. Kraus, *Radio Astronomy*. New York, NY, USA: McGraw-Hill, 1966, ch. 3 & 7.

JACOB W. KOOI (Senior Member, IEEE) was born in Geldrop, The Netherlands, on July 12, 1960. He received the B.S. degree in microwave engineering with the California Polytechnic State University, San Luis Obispo, CA, USA, in 1985, the M.S. degree in electrical engineering from the California Institute of Technology, Pasadena, CA, USA, in 1992, and the Ph.D degree in physics with the Kapteyn Institute for Astronomy, University of Groningen, Groningen, The Netherlands, in 2008. He is currently with the Jet Propulsion Laboratory, California Institute of Technology. His research interests include millimeter and submillimeter wave technology, low energy physics, superconducting electronics, electrodynamics, thermodynamics, low-noise amplifiers and associated device physics, fourier optics, instrument system stability, and their application to astronomy and aeronomy.

MELISSA SORIANO received the B.S. degree from Caltech, Pasadena, CA, USA, double major in electrical and computer engineering and business economics and management, and the M.S. degree in computer science from George Mason University, Fairfax, VA, USA. She is currently a Payload Systems Engineer in communications, tracking, and radar division with the Jet Propulsion Laboratory. She is the Telecom X-band Systems Engineer for Mars Sample Return Lander and the Telecom Lead for the Europa Clipper Flight System Team. She was part of the Direct to Earth EDL Tones Team for M2020 and MSL and also worked on the DSCC Downlink Array and the Wideband VLBI Science Receiver used in the Deep Space Network.

JAMES BOWEN (Member, IEEE) received the B.S. degree in physics from California State University Northridge, Los Angeles, CA, USA, in 1990. Since 1984, he has been with the Jet Propulsion Laboratory building cryogenic amplifiers for the Deep Space Network (DSN). In 1986, he was with MASERs, transitioning to HEMT amplifiers. Since 2005, he has been the Microwave System Engineer for the DSN.

ZUBAIR ABDULLA received the B.Eng. degree in engineering physics from the University of Illinois at Urbana-Champaign, Champaign, IL, USA, in 2009, and the Ph.D. degree in astrophysics from The University of Chicago, Chicago, IL, USA, in 2018. From 2019 to 2022, he was a Postdoctoral Fellow with NASA Jet Propulsion Laboratory (JPL), developing microwave instrumentation for radio astronomy with the Deep Space Network. He is currently a RF Microwave Engineer with NASA-JPL, where his research interests include microwave instrumentation, interferometry, and low-noise amplifiers and their applications to radio astronomy and deep space communications.

LORENE SAMOSKA (Senior Member, IEEE) received the B.S. degree in engineering physics from the University of Illinois at Urbana-Champaign, Champaign, IL, USA, in 1989, and the Ph.D. degree in materials engineering from the University of California, Santa Barbara, Santa Barbara, CA, USA, in 1995. She was a Postdoctoral Researcher of the design and fabrication of state-of-the-art InP HBT microwave digital circuits with the University of California, Santa Barbara. In 1998, she joined the Jet Propulsion Laboratory, where she is currently a Principal Engineer involved in the design and testing of 30–600 GHz HEMT MMIC low noise amplifiers and receivers, and power amplifiers for local oscillator sources and transmitters in future space missions.

ANDY K. FUNG (Member, IEEE) received the B.E.E., M.S.E.E., and Ph.D. degrees in electrical engineering from the University of Minnesota, Minneapolis, MN, USA, in 1993, 1995 and 1999, respectively. His research interests include the development of gallium nitride and indium phosphide MMICs for radars, remote sensing receivers, and laboratory instrumentation.

RAJU MANTHENA received the bachelor's degree in electrical engineering with the University of South Florida, Tampa, FL, USA, and the master's degree in electrical engineering with the University of California, Los Angeles, Los Angeles, CA, USA, where he is currently working toward the Ph.D. degree in physics. He has been working with JPL for the past 5 years focusing on RF systems, electromagnetics, antennas, optical systems, and analog circuits, mainly for NASA's Deep Space Network, and radio astronomy applications. He has also worked on transient magnetic sensing for underground water and has been involved in building a physics package for atom interferometers. His Ph.D. thesis is experimental atomic physics for precision measurements, such as for dark matter and dark energy.

DANIEL HOPPE (Senior Member, IEEE) received the B.S. and M.S. degrees in electrical engineering from the University of Wisconsin-Madison, Madison, WI, USA, and the Ph.D. degree in electrical engineering from the University of California, Los Angeles, Los Angeles, CA, USA. He is currently a Principal Engineer with the Communications Ground Section, Jet Propulsion Laboratory. His research interests include electromagnetic scattering, microwave component design, high power RF systems, and optical communications.

HAMID JAVADI received the Ph.D. degree in physics from the University of California, Los Angeles, Los Angeles, CA, USA, in 1985. His Doctoral research concerned the electrodynamic response of spin density waves in charge transfer inorganic salts. He is currently a member of the Technical Staff with the Jet Propulsion Laboratory (JPL), Pasadena, CA, where he has been involved with diverse areas of microwave characterization of materials, measurement techniques, free-flyer miniature spacecrafts, molecular clocks, millimeter-wave radiometers, THz receivers, and photo mixers.

TIMOTHY CRAWFORD was hired into Jet Propulsion Laboratory (JPL), as an affiliate in 1975, then joined the JPL High Resolution Spectroscopy Lab in 1985. In 1988, he became a JPL employee. Since joining the JPL High Resolution Spectroscopy Lab, he has built numerous in situ and remote sensing instruments. These instruments are utilized in ground based, sub-orbital, and orbital observational platforms for atmospheric research and astronomy.

DARREN J. HAYTON received the B.Sc. degree in planetary and space physics and the Ph.D. degree in materials physics from the University of Wales, Aberystwyth, U.K., in 1998 and 2002, respectively. From 2002 to 2008, he was a Postdoctoral with the Astronomy Instrumentation Group, University of Wales, Cardiff, U.K., developing THz instrumentation for astrophysics and Earth observing applications that include JWST-MIRI and Mars Reconnaissance Orbiter - MCS. From 2010 to 2016, he was an Instrument Scientist with SRON, Groningen, NL, where he worked on superconducting HEB mixers and quantum cascade laser local oscillators. From 2016 to 2022, he was a Technologist with the submillimeter wave advanced Technology Group, Jet Propulsion Laboratory, California Institute of Technology, Pasadena, CA, USA. His current work is with Oxford Quantum Circuits, U.K., developing and deploying multi-qubit quantum computers.

INMACULADA MALO-GÓMEZ was born in Madrid, Spain, in 1972. She received the B.Eng. and Ph.D. degrees in telecommunications engineering from the Universidad Politecnica de Madrid, Madrid, Spain, in 1998 and 2011, respectively. From 1996 to 2002, she worked in radiopropagation and mobile communications with Telefonica and Orange companies. In 2003, she joined the Yebes Observatory, where she has been involved in the development and construction of cryogenic receivers for radio telescopes. Since 2009, she has been with the LNA Laboratory in low-noise amplifier and passive component design for radio astronomy focusing on quadrature cryogenic wideband hybrids.

JUAN DANIEL GALLEGO-PUYOL (Member, IEEE) was born in Madrid, in 1960. He received the Ph.D. degree in physics with the University of Central Missouri, Madrid, Spain, in 1992. He is currently the Head of the instrumentation and Technological Development Department, Yebes Observatory, Spain, and a Member of the URSI and IAU. In 1989, he spent a year with the National Radio Astronomy Observatory, Charlottesville, VI, USA. His main research interests include the development of low noise cryogenic receivers and amplifiers for radio astronomy, deep space communications and instrumentation. He has participated in numerous international projects and contracts in this field. Among others, he has been in charge of the development and construction of the IF cryogenic amplifiers for ESA's Herschel mission and for the European receivers of the Atacama Large Millimeter/submillimeter Array (ALMA).

AHMED AKGIRAY (Senior Member, IEEE) received the B.S. degree (with Hons.) in electrical engineering with Cornell University, Ithaca, NY, USA, in 2005, the M.S. degree in electrical engineering with the University of Illinois at Urbana-Champaign, Champaign, IL, USA, in 2007, and the Ph.D. degree in electrical engineering with the California Institute of Technology, Pasadena, CA, USA, in April 2013. Prior to his Ph.D., he was with NASA's Jet Propulsion Laboratory, as an RF/Microwave Engineer on two spaceflight missions: the Mars Science Laboratory and Soil Moisture Active Passive (SMAP). He is currently an Assistant Professor with Ozyegin University, Istanbul, Turkey, and also the Chief Technology Officer of ALCAN Systems GmbH, a German start-up working on phased array antennas for next generation satellite constellations and 5G networks.

BEKARI GABRITCHIDZE received the M.Sc. degree in advanced physics and the Ph.D. degree in applied physics from the Department of Physics, University of Crete, Rethymno, Greece, in 2017 and 2022, respectively. He completed his Ph.D. work as a Visiting Student with Cahill Radio Astronomy Laboratory (CRAL), California Institute of Technology, Pasadena, CA, USA, where he worked on W-band low noise MMIC design, On-wafer characterization and modelling of HEMTs, where effort was concentrated on the explanation and understanding of the origin of drain noise and the ways of mitigating the overall noise temperatures of HEMTs. He is currently a Research Engineer with CRAL, California Institue of Technology, where his research focuses on the development of low noise HEMTs and MMICs.

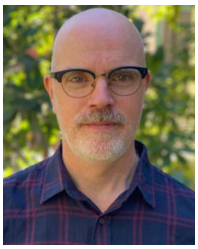

KIERAN A. CLEARY received the M.Eng.Sc. degree in electronic engineering from The National University of Ireland, Dublin, Ireland, in 1994, and the Ph.D. degree in radio astronomy on cosmic microwave background observations using the Very Small Array from The University of Manchester, Manchester, U.K., in 2004. He is currently a Senior Scientist with the California Institute of Technology, Pasadena, CA, leading a spectral line intensity mapping experiment (COMAP) targeting the Epoch of Galaxy Assembly. He leads an effort to optimize the cryogenic performance of amplifiers for radio astronomy with the Cahill Radio Astronomy Laboratory (CRAL). He is also an Associate Director of the Owens Valley Radio Observatory.

CHRISTOPHER JACOBS received the B.S. degree in applied physics from California Institute of Technology, Pasadena, CA, USA, in 1983. He is currently a Senior Engineer with the Deep Space Tracking Systems Group, Jet Propulsion Laboratory, Pasadena. His work has centered on producing inertial reference frames based on observations of extragalactic radio sources. These frames define the angular coordinates used for spacecraft navigation and other applications. He has served on four IAU working groups for the International Celestial Reference Frames (ICRF) which provide the IAU's official system of coordinates on the sky. From 2012 to 2015, he Chaired the ICRF Group. His research focuses on extending the ICRF to higher radio frequency bands at 24, 32, and 43 GHz. Mr. Jacobs is a member of AAS and the President of the IAU commission on astrometry. He is active in professional education and public outreach. He was the recipient of the NASA Medal for Exceptional Achievement in recognition of his work in 2015.

JOSEPH LAZIO received the Ph.D. degree from Cornell University, Ithaca, NY, USA. He is currently the Interplanetary Network Directorate Scientist with the Jet Propulsion Laboratory, California Institute of Technology, Pasadena, CA, USA, and a Project Scientist for the Sun Radio Interferometer Space Experiment. The Interplanetary Network Directorate manages the Deep Space Network for NASA's Space Communications and Navigation (SCaN) Program. He was an U.S. National Research Council Research Associate with the U.S. Naval Research Laboratory, and was a Radio Astronomer on the staff of the U.S. NRL, before joining JPL. He was the Deputy Principal Investigator for the proposed Dark Ages Radio Explorer. He was the Project Scientist for the Square Kilometre Array, the Deputy Director of the Lunar University Network for Astrophysics Research, and a Project Scientist for the U.S. Virtual Astronomical Observatory. He observes routinely with the world's premier ground-based radio telescopes, including the Karl G. Jansky Very Large Array and the Very Long Baseline Array.